Evaluating magmatic additions at a magma-poor rifted margin: An East Indian case study

Caroline Harkin, Nick Kusznir, Julie Tugend, Gianreto Manatschal, Ken Mcdermott

Geophysical Journal International

Geophys. J. Int. (2019) **217,** 25–40
Advance Access publication 2019 January 9
GJI Geodynamics and tectonics

doi: 10.1093/gji/ggz007

Evaluating magmatic additions at a magma-poor rifted margin: an East Indian case study

Caroline Harkin [1], Nick Kusznir [1], Julie Tugend [2,3] Gianreto Manatschal [4] and Ken McDermott[5]

[1] *Department of Earth, Ocean and Ecological Sciences, University of Liverpool, Liverpool L693GP, UK E-mail: C.Harkin@liverpool.ac.uk*
[2] *Sorbonne Université, CNRS-INSU, Institut des Sciences de la Terre, ISTeP UMR 7193, F-75005 Paris, France*
[3] *Total SA, R&D Departement CSTJF, Pau, France.*
[4] *Institut de Physique du Globe de Strasbourg; CNRS-UMR* 7516, *Université de Strasbourg,* 1 *rue Blessig, F-*67084 *Strasbourg Cedex, France*
[5] *ION,* 31 *Windsor Street, Chertsey KT*168*AT, UK*

Accepted 2019 January 7. Received 2019 January 3; in original form 2018 January 10

SUMMARY

Rifted margins are often classified as magma-poor or magma-rich based on a magmatic budget interpretation from seismic reflection data. The southern segment of the East Indian rifted margin is often regarded as a type-example of a magma-poor margin displaying exhumed mantle. However, in its southern segment, 9 km thick transitional crust, previously interpreted as magmatic crust, separates the exhumed mantle from thin oceanic crust. Such thick transitional crust is atypical for a magma-poor margin, so we investigate its likely formation and potential implications for the evolution of magma-poor margins. Using an integrated set of geophysical techniques alongside seismic reflection data, we test the existence of exhumed mantle and the composition of the transitional crust. These geophysical techniques consist of gravity inversion, residual depth anomaly analysis, flexural subsidence analysis and joint inversion of gravity and seismic data. We apply these methods to high-quality seismic reflection data (ION line INE1-1000) on the southern segment of the East Indian rifted margin and test a series of geological scenarios for the margin structure using our integrated quantitative analysis. Of these, our quantitative analysis, seismic observations and the regional plate kinematic history support a structure consisting of thinned continental crust inboard of exhumed, serpentinized mantle followed by thick (∼9 km) magmatic crust transitioning into thin oceanic crust (∼5 km). The juxtaposition of exhumed mantle and thick magmatic crust is explained by the occurrence of a jump in seafloor spreading during the Early Cretaceous formation of the south-east Indian Ocean. The final rifted margin structure contains characteristics of both magma-poor and magma-rich rifted margins resulting from two distinct rift events with different magmatic budgets. The investigation of the East Indian rifted margin structure and evolution shows the importance of incorporating the plate kinematic history and quantitative validation of seismic interpretation into the analysis. Classifying the East Indian margin as a typical magma-poor rifted margin is misleading causing us to question the use of end-member terminology to describe rifted margins.

Key words: geodynamics; rifted margin; gravity anomalies; reflection seismology.

1 INTRODUCTION

The classification of rifted margins commonly falls into two end-member types, magma-poor and magma-rich (e.g. Boillot *et al.* 1989; Pickup *et al.* 1996; Geoffroy 2005; Reston 2009; Reston & Manatschal 2011; Franke 2013), using an estimation of the volume of magmatic additions based on seismic interpretations with little to no quantitative assessment. Resolving the magmatic budget based on seismic reflection observations can be ambiguous, leading to several potential interpretations of the magmatic volume (Tugend *et al.* 2018), with different implications for rifted margin formation processes. By definition, a magma-poor rifted margin is characterized by relatively small amounts of magmatic additions. In some cases, this leads to the rupture and separation of continental crust and consequent mantle exhumation before the onset of decompression melting and seafloor spreading. The delay in the onset of decompression melting, with respect to crustal rupture may be due to depleted or cool mantle or slow spreading rates (Fletcher

et al. 2009; Lundin & Doré 2011; Pérez-Gussinyé 2013; Doré & Lundin 2015). Alternatively, there may be an initial retention of melt (Lizarralde *et al.* 2004) until a critical melt threshold is exceeded. The formation processes of magma-poor rifted margins and mantle exhumation have been extensively investigated on the Iberian margin by deep-sea drilling and seismology. During the development of these rifted margins, once continental crust is thinned to less than 10 km the entire crust becomes embrittled and is termed 'hyper-extended' (Pérez-Gussinyé *et al.* 2006; Sawyer *et al.* 2007; Reston 2009; Sutra *et al.* 2013; Tugend *et al.* 2015). Embrittlement of the crust allows for faults to penetrate into the underlying mantle, transporting fluids and leading to the serpentinization of the mantle underneath hyper-extended crust (Tucholke *et al.* 2008; Reston 2009; Pérez-Gussinyé 2013; Doré & Lundin 2015; Gillard *et al.* 2016). Seismic velocities for exhumed, serpentinized mantle range from 5 to 8 km s^{-1} (Reston 2009) with depth-dependent densities ranging from 2650 to 2850 kg m^{-3} at the surface, to 3000 kg m^{-3} at depth, depending on the amount of magnetite present (Cooper 2010). The transition between exhumed mantle and first oceanic crust is believed to occur when the rise of the asthenosphere is enough to generate decompression melting that initiates seafloor spreading (Tucholke *et al.* 2007) with average oceanic crust that has a thickness of 7 km (White *et al.* 1992) and an average basement density of 2860 kg m^{-3} (Carlson & Herrick 1990).

The East Indian rifted margin (Fig. 1) has previously been classified as magma-poor following seismic interpretations of high-quality seismic reflection data, such as seismic line INE1-1000 (Fig. 2) and others from ION Geophysical, that deduce the presence of hyperextended continental crust and exhumed mantle (Nemčok *et al.* 2013; Pindell *et al.* 2014; Sinha *et al.* 2015; Haupert *et al.* 2016; Tugend *et al.* 2018). In addition, these seismic interpretations show an ∼9 km thick transitional crust separating exhumed mantle and thin oceanic crust. The juxtaposition of mantle exhumation, thick transitional crust and thin oceanic crust poses an interesting question for the evolution of a supposedly typical magma-poor rifted margin during breakup, the initiation of decompression melting and the extraction of that melt to form oceanic crust. In order to investigate this enigma, we carry out validations of these previous interpretations.

We test the presence of exhumed mantle and investigate the composition of the transitional crust using a set of quantitative methods: gravity inversion, residual depth anomaly analysis, subsidence analysis and joint inversion of gravity and seismic data. We also provide and examine alternative geological interpretations based on seismic observations and quantitative analyses with the aim of better understanding the tectonic and magmatic structures present at rifted margins and the magma-poor versus magma-rich classification of rifted margins.

1.1 Geological background

1.1.1 Formation of the East Indian rifted margin

The East Indian rifted margin formed as a result of a polyphase breakup between India and Antarctica (Ramana *et al.* 1994, 2001; Frey *et al.* 2000; Chand *et al.* 2001; Gaina *et al.* 2003, 2007; Lal *et al.* 2009; Radhakrishna *et al.* 2012; Gibbons *et al.* 2013; Sinha *et al.* 2015) and now consists of a series of segmented basins which from north to south are the Bengal Basin, Mahanadi Basin, Krishna–Godavari Basin and the Cauvery Basin (Lal *et al.* 2009; Fig. 1a). The complex evolution of extensional deformation related to breakup and the formation of the East Indian rifted margin is associated with the creation of a microcontinent, Elan Bank. This microcontinent currently lies in the Enderby Basin, the conjugate to the East Indian margin, as part of the Kerguelen Plateau (Müller *et al.* 2001; Nicolaysen *et al.* 2001; Ingle *et al.* 2002a; Borissova *et al.* 2003; Gaina *et al.* 2003, 2007; Sinha *et al.* 2015). Geochemical, petrological, seismic and potential field evidence suggests Elan Bank was situated adjacent to East India within the Krishna–Godavari Basin prior to lithospheric breakup (Charvis *et al.* 1995; Charvis & Operto 1999; Frey *et al.* 2000; Nicolaysen *et al.* 2001; Ingle *et al.* 2002a; Borissova *et al.* 2003; Gaina *et al.* 2003, 2007).

In this study we refer to lithospheric breakup as the point where seafloor spreading has initiated after the separation of continental crust and the rise of the underlying lithosphere (Soares *et al.* 2012).

Due to the polyphase and complex nature of breakup along the East Indian rifted margin, it has been suggested that lithospheric breakup between India, Elan Bank and Antarctica occurred in two stages separated by an ocean ridge jump. Initially, seafloor spreading occurred between India/Elan Bank and Antarctica. The age of lithospheric breakup and seafloor spreading is debated, with ages based on both magnetic anomaly evidence and plate reconstructions. Magnetic anomaly M11, present in Enderby Basin (Ramana *et al.* 2001), implies that seafloor spreading was active at 134 Ma. However, Sinha *et al.* (2015) used plate reconstructions to suggest that the breakup between India/Elan Bank and Antarctica occurred at 132 Ma. Other magnetic anomalies found in the Enderby Basin M9o to M2o suggest seafloor spreading between India/Elan Bank and Antarctica occurred from 130.2 to 124.1 Ma (Gaina *et al.* 2007).

An ocean ridge jump northwards, to between India and Elan Bank, then leads to a second stage of rifting with a proposed lithospheric breakup age ranging between 124 and 120 Ma. Evidence for an ocean ridge jump comes from south of Elan Bank, where magnetic lineations in oceanic crust show a fossilized spreading centre that became extinct after the formation of magnetic anomaly M2 at 124 Ma (Müller *et al.* 2001; Borissova *et al.* 2003; Gaina *et al.* 2007). Apart from limited magnetic lineations, there is little geophysical evidence for the age of breakup; however some studies use plate reconstructions to show that breakup occurred at ∼120 Ma (Royer & Coffin 1988; Müller *et al.* 2000).

Around the time of lithospheric breakup between India and Elan Bank, magmatic events in the Bay of Bengal produced large volumes of extrusive material (Frey *et al.* 2000; Coffin *et al.* 2002; Ingle *et al.* 2002b; Olierook *et al.* 2016). These events were associated with asthenosphere temperature anomalies linked to the Kerguelen plume, occurring as early as 137 Ma through to the present day (Olierook *et al.* 2016).

1.1.2 Previous work on INE1-1000

Previous studies have analysed seismic reflection data on the East Indian rifted margin (Fig. 1b) including ION line INE1-1000 (Fig. 2), which is the focus of this paper. These studies give interpretations of the regional tectonic history based predominantly on seismic data, with the addition of other methods such as forward gravity modelling (Nemčok *et al.* 2013).

Nemčok *et al.* (2013) discussed the presence of exhumed mantle along the East Indian rifted margin with a thin layer of volcanic cover that was unroofed from beneath the proximal continental crust along certain segments of the margin. In particular, on seismic line INE1-1000, the exhumed mantle was shown to be adjacent to an area of thick crust (∼9 km) defined as the proto-oceanic corridor that varies

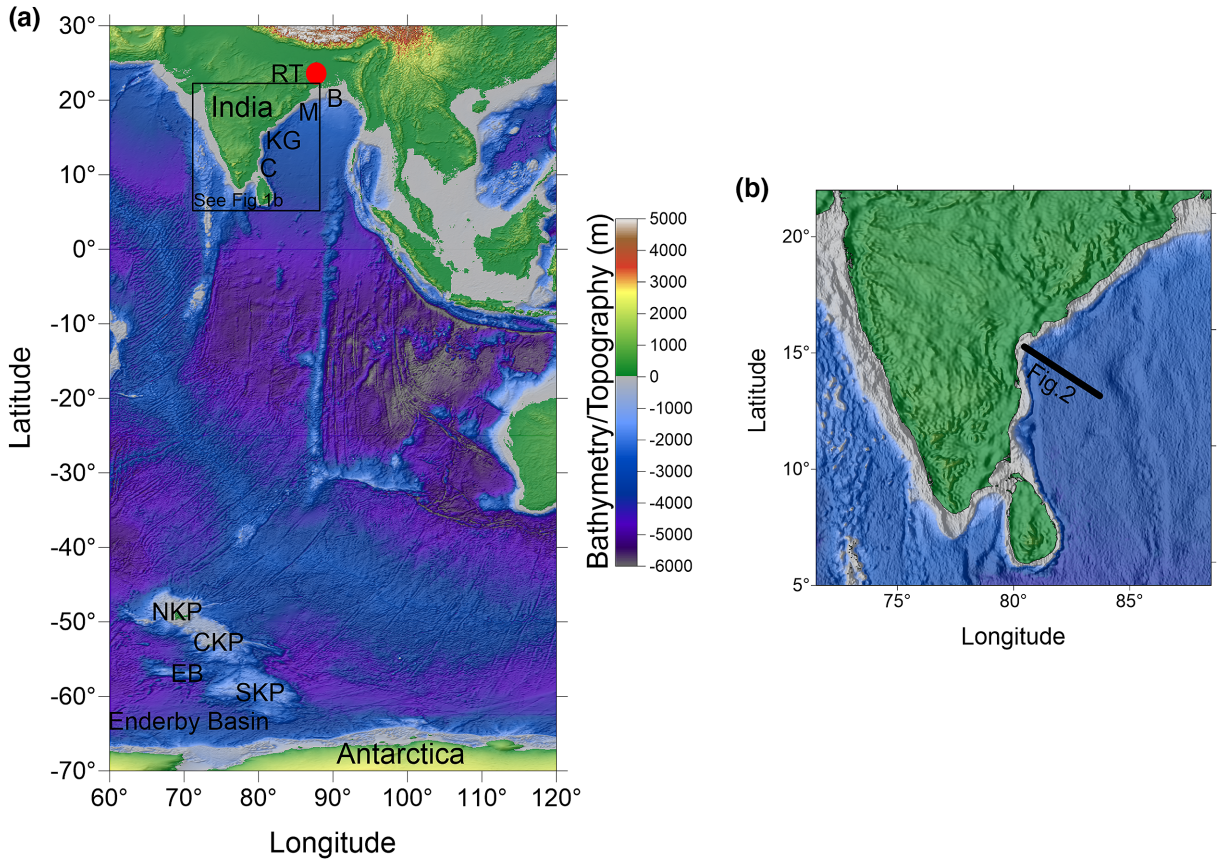

Figure 1. (a) Bathymetry/topography map of India, Antarctica and the Indian Ocean (Smith & Sandwell 1997) with an overlay of free-air gravity anomaly shaded relief (Sandwell & Smith 2009); B, Bengal Basin; C, Cauvery Basin; CKP, Central Kerguelen Plateau; EB, Elan Bank; KG, Krishna–Godavari Basin; M, Mahanadi Basin; NKP, North Kerguelen Plateau; RT, Rajmahal Traps; SKP, South Kerguelen Plateau. (b) Enlargement of box shown in (a) with location of seismic profile shown in Fig. 2.

in thickness from 4.2 to 11.2 km before terminating to form oceanic crust with an average thickness of 5.4 km. Proto-oceanic crust is here defined as magmatic crust that does not yet display all the properties and characteristics of normal oceanic crust. Nemčok *et al.* (2013) used gravity forward modelling with densities for the proto-oceanic crust varying between 2.99 and 3.13 g cm^{-3} representing a combination of seaward dipping reflectors, exhumed mantle and continental fragments resulting from disorganized seafloor spreading. Sinha *et al.* (2015) is in agreement with Nemčok *et al.* (2013) with the interpretation of exhumed mantle and thick crust as part of a proto-oceanic corridor using adjacent seismic profiles. However, they focus on the formation of Elan Bank as a microcontinent, stating that the margin of Elan Bank also contains proto-oceanic crust that matches in seismic reflectivity to the East Indian margin. Pindell *et al.* (2014) also interpreted the presence of serpentinized mantle on INE1-1000 but suggested it is in direct contact with sediments and/or continental crust stratigraphically above, rather than volcanics, with the outboard thick crust being termed oceanic crust, but with the same properties as the proto-oceanic crust described by Nemčok *et al.* (2013) and Sinha *et al.* (2015). Haupert *et al.* (2016) focused on the continental thinning and mantle exhumation of INE1-1000 showing a series of continental faults that accommodate thinning over a distance of 90 km. They show a top basement surface that lies above a narrow band of parallel reflectivity on top of exhumed mantle. A breakup point is defined at the distal edge of the exhumed mantle, at the onset of thick crust, which is considered to be part of the oceanic domain.

2 SEISMIC OBSERVATIONS

Seismic reflection ION line INE1-1000 is situated on the East Indian rifted margin (Fig. 1b) as part of the IndiaSPAN survey from ION Geophysical. Both pre-stacked time and depth migrated seismic reflection profiles (Fig. 2) were interpreted and analysed with each reaching 16 s two-way traveltime (TWTT) and 25 km, respectively.

Here we use first-order seismic observations to define the position of seismic interfaces such as top basement and seismic Moho. Our interpretation of this line follows a methodology similar to that presented in Tugend *et al.* (2018). Top basement is defined as the base of passive infill or the base of syn-rift sediments, and the top of crystalline basement/pre-rift sediments. We define seismic Moho as the deepest continuous visible reflector, which we assume corresponds to the base of the petrological crust, using Warner (1987) as a guide within the time domain to constrain our Moho picks to within 10 ± 1 s TWTT. In addition to identifying seismic interfaces, we investigate the internal seismicity of the proposed basement. We categorize seismic reflections as magmatic intrusions based on work done by Magee *et al.* (2015, 2018), Schofield *et al.* (2012) and Planke *et al.* (2005).

The top basement surface can be traced throughout the seismic reflection profile. Over the proximal domain from a line-distance of 0–7 km, top basement deepens by ∼7 km, cut by a series of seaward dipping faults. From a line-distance of 75 km to 120 km, there are two candidates for top basement. The first possible top

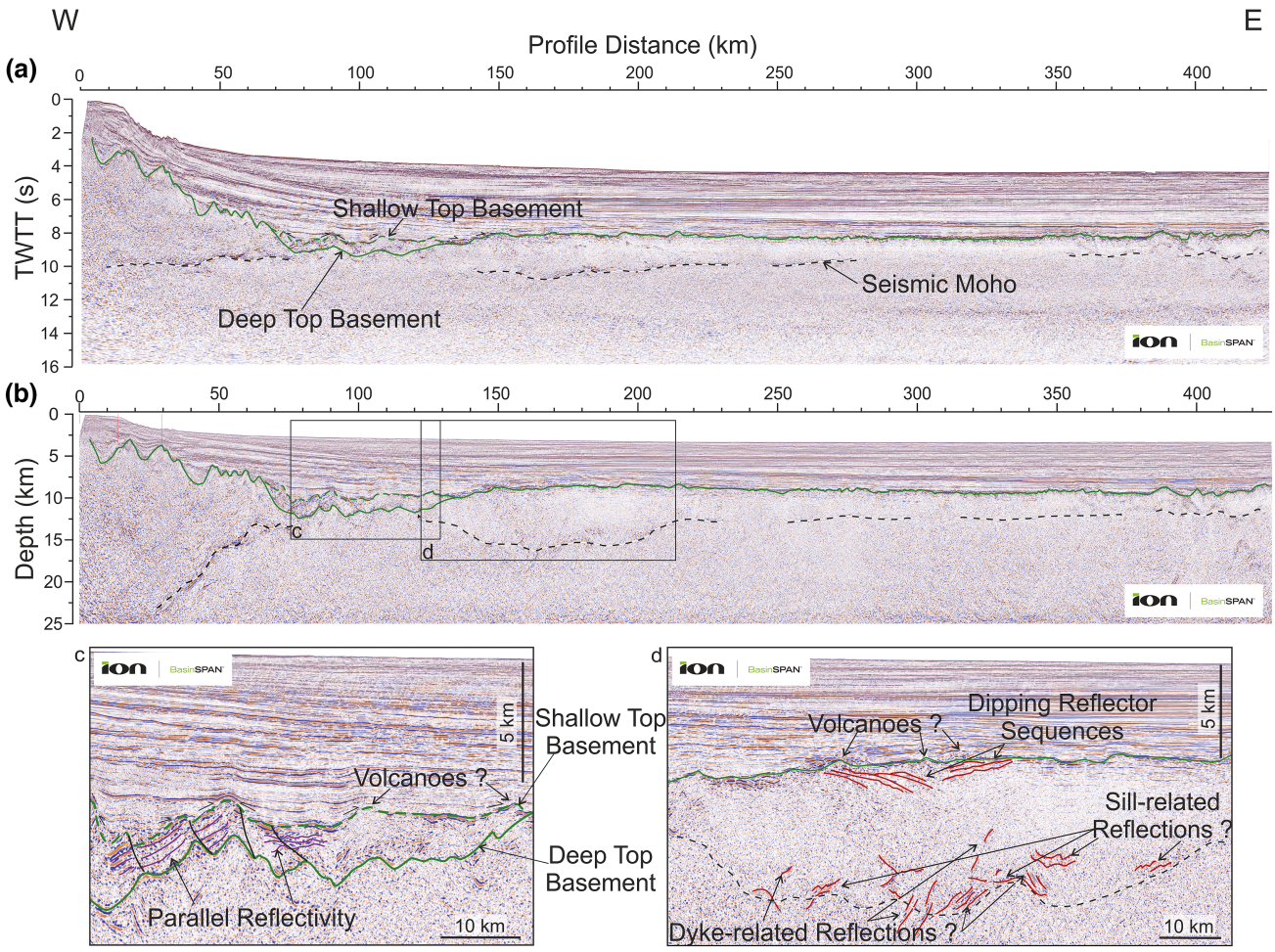

Figure 2. Seismic observations of INE1-1000 location shown by Fig. 1(b). (a) Pre-stacked time migrated (PSTM) seismic reflection profile showing top basement surfaces (shallow top basement, dashed green and deep top basement, solid green) and seismic Moho (dashed white and black). (b) Pre-stacked depth migrated (PSDM) seismic reflection profile showing top basement surfaces (shallow top basement, dashed green and deep top basement, solid green) and seismic Moho (dashed white and black). (c) Enlargement of box in (b) showing two top basement surfaces over region of presumed exhumed mantle. Parallel reflectivity between the two surfaces is highlighted. (d) Enlargement of box in (b) showing area of thick crust. Volcanic and magmatic features are highlighted, e.g. intrusions, submarine volcanoes and dipping reflector sequences. Within the central region of the thick crust there is a lack of any clear internal reflections.

basement surface lies at a depth of 8.5–10 km at the base of passive infill, characterized by onlap and downlap geometries of the overlying sediments, similar to the top basement surface presented in Nemčok *et al.* (2013), Haupert *et al.* (2016) and Pindell *et al.* (2014; shallow top basement surface, Fig. 2). The second possible top basement surface is situated at the base of a reflective package stratigraphically below the passive infill at a depth of ∼12 km similar to the top basement shown by Tugend *et al.* (2018; deep top basement surface, Fig. 2). Within the package, reflectivity shows sub-parallel layers that are offset from one another periodically and that downlap onto the base of the package (Fig. 2c). Depending on the nature of underlying basement, the parallel-bedded reflectors are either pre-rift sediments formed on existing continental crust or post-rift sediments deposited on newly formed basement (i.e. exhumed mantle or magmatic basement). From a line-distance of 120 to 220 km, top basement depth shallows to ∼7.5 km where reflectors are largely continuous from the surface. These reflectors are interrupted by volcanoes that extend into the overlying, onlapping sediments (Fig. 2d). From a line-distance of 220 to 380 km, top basement is parallel to bathymetry with little to no topography and is represented by a series of short, discontinuous reflectors. At the end of the profile, from line-distance 380 km onwards, top basement topography forms dome-like structures. From these first-order observations, there are two possible top basement interfaces that will be tested in this study, which vary in depth between line-distances of 75 and 120 km (Fig. 2c).

Seismic Moho from a line-distance of 0 to 75 km shows a continuous reflector that shallows rapidly, merging with the base of the parallel-bedded reflective package at a line-distance of 75 km. Between line-distances 75 and 120 km, there is no visible seismic Moho. The deepest reflector here is the base of the reflective package at ∼12 km. Seismic Moho is once again visible from a line-distance of ∼120 km, at a depth of ∼16 km where it forms a succession of discontinuous reflectors. From a line-distance of 200 to 220 km seismic Moho begins to shallow once more to ∼12 km and from line-distance 220 km to the end of the profile it remains sub-parallel to the top basement surface. It should be noted that the seismic Moho is more visible on the PSTM seismic section (Fig. 2b).

Between a line-distance of 120 and 220 km, the crust is ∼9 km thick and is the thick crustal area under investigation. In the lower section of the basement, there is seismic evidence for a number of intrusions (Fig. 2d), including step geometries that are indicative of

sill complexes and sub-vertical dyke-related reflections (Magee *et al*. 2015, 2018). In the top portion of the crust, dipping reflector sequences that dip both seawards and landwards can be seen (Fig. 2d) features commonly associated with volcanic activity.

3 METHODS

3.1 Gravity anomaly inversion

Depth to the Moho, crustal thickness and lithosphere thinning have been calculated using the gravity anomaly inversion (Greenhalgh & Kusznir 2007; Alvey *et al.* 2008; Chappell & Kusznir 2008; Roberts *et al.* 2013; Cowie *et al.* 2015; Kusznir *et al.* 2018). We use bathymetry data from Smith & Sandwell (1997) alongside satellite-derived free-air gravity from Sandwell & Smith (2009). Ocean age isochrons are taken from Müller *et al.* (1997) and 2-D sediment thickness is calculated from pre-stacked depth-migrated seismic reflection data on the East Indian rifted margin.

We perform the inversion in the 3-D spectral domain to give 3-D Moho geometry using the method of Parker (1972) and invoking Smith's theorem (Smith 1961) to provide a unique solution for the assumptions made. We use a constant crustal density of 2850 kg m^{-3} (averaged from Carlson & Herrick 1990; Christensen & Mooney 1995). Continental rifted margins and oceanic lithosphere have an elevated geotherm (Chappell & Kusznir 2008) that results in a large negative mass deficiency and lithosphere thermal gravity anomaly. Our gravity inversion incorporates a correction for this lithosphere thermal gravity anomaly; without this correction Moho depth would be overestimated.

The lithosphere thermal anomaly correction is determined from present-day lithosphere temperatures calculated using a 3-D lithosphere thermal model. Cooling times for oceanic lithosphere are derived from ocean isochrons, while cooling time for rifted continental margin lithosphere uses the breakup age (Chappell & Kusznir 2008). The initial thermal perturbation of rifted continental margin lithosphere is derived from the lithosphere thinning factor, γ, calculated in the gravity inversion. For oceanic lithosphere $\gamma = 1.0$. The lithosphere thinning factor, γ, is defined as $\gamma = 1-1/\beta$, where β is the lithosphere stretching factor (McKenzie 1978). For rifted margin lithosphere, β is determined from the ratio of initial continental crustal thickness to present-day continental crustal thickness. Lithosphere thinning and crustal thinning are taken to be equivalent assuming depth-uniform stretching and thinning.

We investigate the sensitivity to breakup age using rounded values of 130 and 120 Ma that correspond to the breakup ages of the two rift phases discussed earlier. Due to the uncertainty in the breakup ages for each rift phase, we also investigate breakup ages of 135 and 115 Ma. Tests show that the depth to the Moho produced by the gravity inversion (Fig. 3a) is not significantly dependent on the breakup age.

3.1.1 *Reference Moho depth calibration*

The calculation of Moho depth from gravity inversion requires a reference Moho depth. Reference Moho depth is dependent on the long wavelength gravity field that is controlled by deep mantle processes, which vary globally, not by crustal or lithosphere density structure. It is important that this reference Moho depth is calibrated. In the absence of seismic refraction data, we have calibrated the reference Moho depth against the seismic oceanic Moho. We use a reference Moho depth of 35 km in the gravity inversion that gives Moho depths which, when taken into the time domain, closely match the seismic Moho visible oceanwards on the TWTT seismic section (Figs 2 and 3b).

3.1.2 *Sensitivity to magmatic addition*

During rifting, magmatic material resulting from decompression melting may be added to the crust in the form of extrusives and intrusives. Determining the remaining thickness of continental crustal basement at rifted margins is required in order to locate the distal limit of continental crust and to calculate the lithosphere thinning factor from the gravity inversion. Furthermore, the amount of magmatic addition and the timing of its initiation with respect to breakup is highly variable at rifted margins, as testified by the differences between magma-poor and magma-rich rifted margins. While the gravity inversion gives the total thickness of crustal basement, it cannot alone distinguish continental basement from new magmatic material that eventually forms oceanic crust.

Within the gravity inversion we regard the degree of decompression melting (e.g. magma-poor, 'normal', magma-rich) as an *a priori* assumption and test for each end-member scenario. The thickness of magmatic addition is determined from lithosphere thinning factor using a parametrization of the decompression melting models of McKenzie & Bickle (1988) and White & McKenzie (1989). This parametrization is discussed in more detail in Chappell & Kusznir (2008).

Fig. 3(c) shows the lithosphere thinning factor profiles determined from gravity inversion for a range of decompression melt parametrizations, spanning magma-poor to magma-rich. The corresponding crustal cross-sections are shown in Fig. 3(d) where we see the various partitioning of crustal basement into remnant continental crust and new magmatic crust depending on the melt parametrization used. Note that for the crustal cross-sections, the entire volume of magmatic addition is added as underplated material. In reality, the magmatic addition would be a combination of intrusive and extrusive material. In Figs 3(c) and (d) we examine three different parametrizations of decompression melting; (i) 'normal' magmatic, (ii) magma-poor and (iii) magma-rich. The associated critical thinning factors for the onset of decompression melting and maximum magmatic addition (final oceanic crust thickness) are summarized in Table 1. An additional parametrization appropriate to serpentinized mantle is also shown in Figs 3(c) and (d) (see Cowie *et al.* 2015 for greater detail).

None of the lithosphere thinning factor profiles and crustal cross-section shown in Figs 3(c) and (d) are geologically plausible or applicable across the whole profile because the parametrization of decompression melt for each end-member scenario does not apply across the whole section. However, each parametrization is applicable for part of the section. We identify where the parametrizations may be applicable and where they are not.

Decompression melt solutions for a top basement pick at the base of passive infill (shallow top basement) have also been calculated (see Supporting Information).

3.2 Residual depth anomaly analysis

The residual depth anomaly (RDA) analysis identifies anomalous bathymetries compared against expected bathymetric anomalies as calculated from thermal plate model predictions from Crosby & McKenzie (2009). In order to calculate the RDA, the difference between the observed bathymetry (b_{obs}, Fig. 4a) and predicted

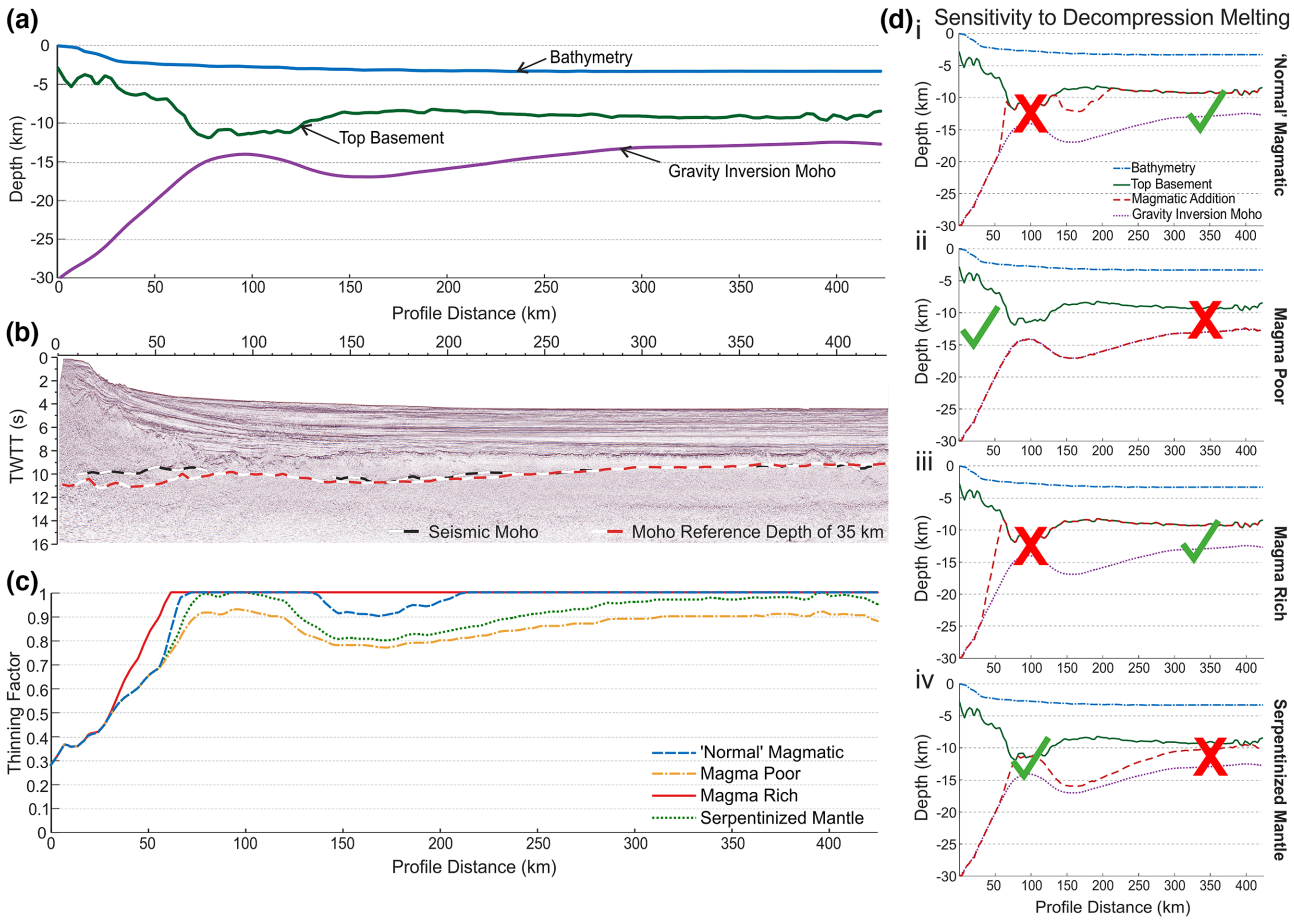

Figure 3. Gravity anomaly inversion results, calibration, and sensitivity to decompression melting. (a) INE1-1000 crustal cross-section showing bathymetry, the deep top basement surface and the gravity inversion Moho without decompression melting. When decompression melt parametrizations are included the depth to the gravity inversion Moho remains unchanged. (b) Comparison of gravity inversion Moho, with a reference depth of 35 km, and observed seismic Moho, for calibration of Moho reference depth. (c) Lithosphere thinning factors generated for each decompression melt parametrization listed in (d) and Table 1. (d) Cross-section profiles of INE1-1000 for each decompression melting scenario: (i) 'normal' magmatic, (ii) magma-poor, (iii) magma-rich and (iv) serpentinized mantle. The ticks indicate areas that match seismic observations and the crosses indicate areas that do not match with seismic observations.

Table 1. Rifted margin end-member gravity inversion parameters

Margin type	Critical thinning factor (γ)	Max. oceanic crustal thickness (km)
'Normal' Magmatic	0.7	7.0
Magma-Poor	0.7	0.0
Magma-Rich	0.5	10.0
Serpentinized Mantle	0.7	3.1

bathymetry (b_{pre}, Fig. 4a) is taken.

$$RDA = b_{obs} - b_{pre} \quad (1)$$

Sensitivities to alternative thermal plate model predictions of b_{pre} have been discussed in Cowie *et al.* (2015) and are shown to have little variation.

The use of sediment-corrected bathymetry in the calculation of the RDA is important as it removes the effect of sediment loading on the basement. The sediment-corrected bathymetry was calculated using flexural backstripping (Kusznir *et al.* 1995) and sediment decompaction assuming shaly-sand compaction parameters (Sclater & Christie 1980).

A negative RDA, whether it is a raw RDA or sediment-corrected RDA, is indicative of crust thinner than the global average of 7 km (White *et al.* 1992). A positive RDA indicates that the crust is thicker than the global average of 7 km.

We also compare the RDA component from crustal basement thickness variations (RDA_{CT}; Cowie *et al.* 2015; Fig. 4b). By observing the difference between the sediment-corrected RDA and the RDA_{CT}, the effect of present-day mantle dynamic topography can be quantified, where a positive difference is representative of mantle dynamic uplift and a negative difference implies mantle dynamic subsidence.

3.2.1 *Sensitivity to breakup age*

As a result of the complex, polyphase breakup between India/Elan Bank and Antarctica, the age of lithospheric breakup is uncertain. Müller *et al.* (2008) gives global ocean age isochrons based on magnetic anomalies but due to the uncertainty in magnetic anomalies dating, it is necessary to consider alternate breakup ages that fit within the uncertainty estimates. Therefore, the sensitivity to lithospheric breakup ages of 115, 120, 130 and 135 Ma (as used in the gravity inversion), in addition to Müller isochrons were calculated and are shown in Fig. 4(c). There is little variation between results, so no preferred lithospheric breakup age can be identified. We use

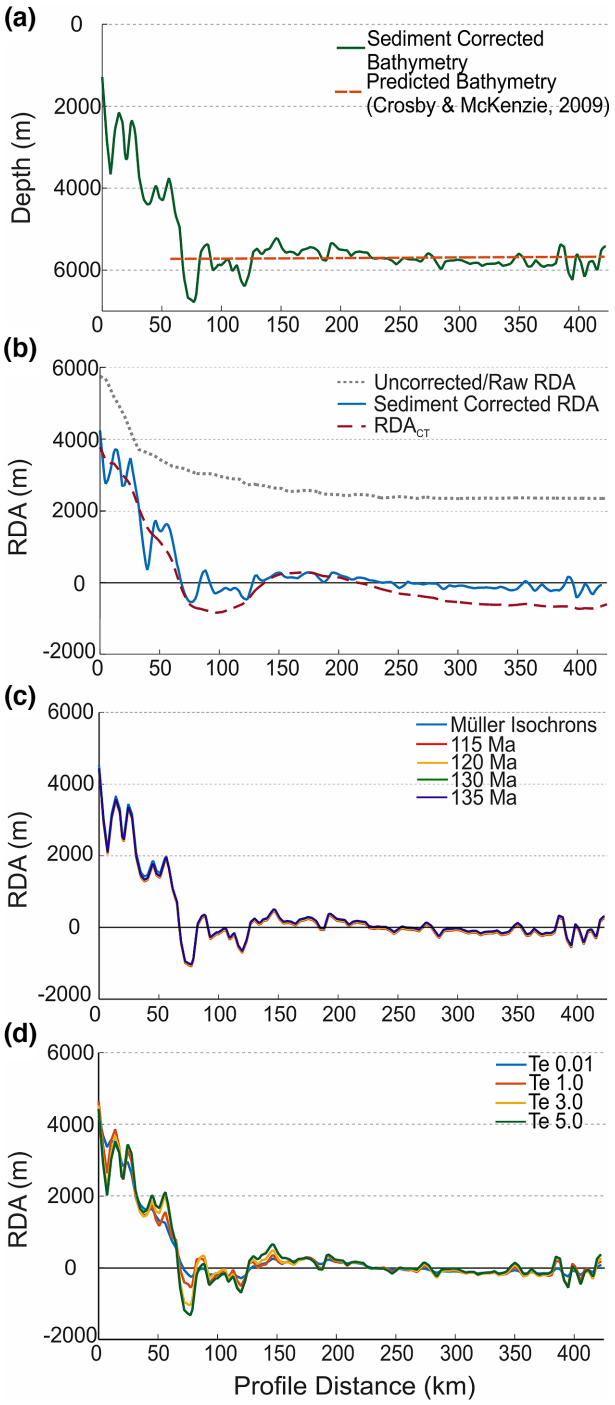

Figure 4. Residual depth anomaly analysis. (a) Cross-section showing sediment-corrected bathymetry and the predicted bathymetry from Crosby & McKenzie (2009). (b) RDA results for uncorrected RDA (black, dotted), sediment-corrected RDA (blue, solid) and crustal basement thickness variation component RDA (red, dashed) using deep top basement surface. (c) Age sensitivity test for seismic line INE1-1000 using Müller isochrons and constant breakup ages of 115, 120, 130 and 135 Ma. (d) Effective elastic thickness (T_e) sensitivity test for seismic line INE1-1000 using T_e of 0.01, 1, 3 and 5 km.

Müller isochrons (Müller *et al.* 2008) in our RDA calculations as there is no notable difference.

3.2.2 *Sensitivity to effective elastic thickness*

Sensitivity to effective elastic thickness (T_e) was investigated using T_e values of 0.01, 1.0, 3.0 and 5.0 km. T_e controls the flexural strength of the lithosphere that depends on many factors (Kusznir & Karner 1985). T_e can vary from margin to margin and often lies in the range of 1.5 to 5 km (Roberts *et al.* 1998). Our results show some variation (Fig. 4d) but it is not significant in changing the overall result. A T_e of 3.0 km was used to calculate the sediment-corrected bathymetry and subsequent RDA results.

3.3 Subsidence analysis

Lithosphere thinning factors can also be calculated using subsidence analysis and are independent to those determined from gravity inversion. Flexural backstripping and decompaction assuming shaly-sand parameters (Sclater & Christie 1980) removes sedimentary layers and loading to the top of the pre-rift sequence and top of oceanic crust, giving a sediment-corrected bathymetry, not an estimate of palaeobathymetry. Sediment-corrected bathymetry approximates water-loaded subsidence if the top of the pre-rift sequence is assumed to have been at sea level prior to rifting. Water-loaded subsidence is assumed to be a combination of initial (S_i) and thermal subsidence (S_t; McKenzie 1978). We convert water-loaded subsidence into thinning factors with the inclusion of a correction for the addition of new magmatic material from decompression melting using a parametrization melt model of White & McKenzie (1989). Magmatic addition results in thicker crust that isostatically reduces the initial subsidence. For the same water-loaded subsidence, the subsidence analysis therefore gives a higher thinning factor. We parametrize decompression melting using the same method as in the gravity inversion (section 3.1.1 and Fig. 3d). An example of the relationship between water-loaded subsidence and thinning factor is shown in Fig. 5(a) for 'normal' decompression melting that produces 7 km thick oceanic crust. As with the gravity inversion, depth-uniform thinning is assumed. The methodology is described in greater detail in Roberts *et al.* (2013) and Cowie *et al.* (2015).

The lithosphere thinning factor profiles produced by subsidence analysis assuming magma-rich, 'normal' and serpentinized mantle are shown in Fig. 5(b). The lithosphere thinning factor can be used to establish the oceanward boundary of continental crust and therefore the location of the continent–ocean boundary. A thinning factor of 1.0 suggests complete thinning of continental crust to the point where no continental crust remains while a low thinning factor of 0.0 suggests no thinning has taken place and the thickness of the continental crust is the initial amount.

3.3.1 *Sensitivity to magmatic addition*

As mentioned previously, Fig. 5(b) displays the lithosphere thinning factor profile determined from subsidence analysis for a magma-rich decompression melt parametrization. For the same water-loaded subsidence as the 'normal' decompression melt, the greater amount of magmatic addition gives a higher thinning factor and implies reduced remnant continental crust. Fig. 5(b) also shows the lithosphere thinning factor profile for a parametrization that represents the serpentinization of exhumed mantle. Serpentinized mantle has been shown to have the equivalent mass deficiency as 3 km thick

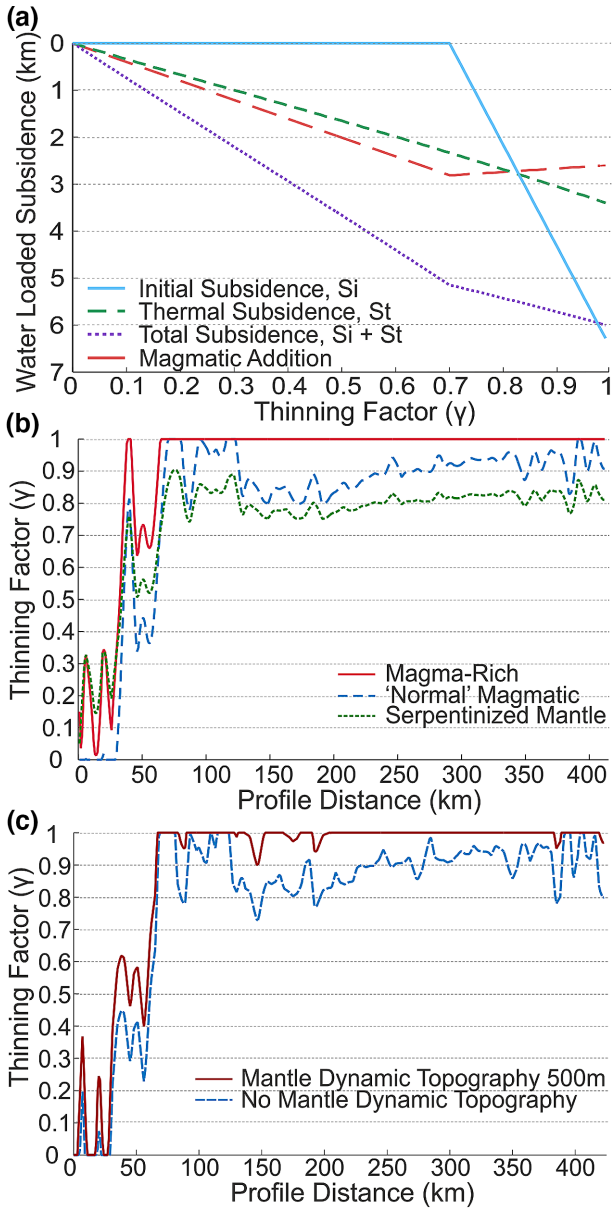

Figure 5. Subsidence analysis: (a) Water-loaded subsidence as a function of thinning factor predicted from McKenzie (1978) modified to include 'normal' decompression melting. (b) Lithosphere thinning factors calculated from subsidence analysis for INE1-1000 for a magma-rich, a 'normal' magmatic solution and a serpentinized mantle solution. (c) 'Normal' magmatic thinning factor from subsidence analysis showing the effect of 500 m of mantle dynamic topography.

crustal basement (Cooper 2010). The detailed explanation of how this can be used for subsidence analysis over serpentinized mantle is given in Cowie *et al.* (2015).

3.3.2 Sensitivity to present-day dynamic topography

Subsidence analysis is an independent way of calculating the lithosphere thinning factor from the gravity inversion but does not directly compensate for mantle dynamic topography. If a margin is experiencing mantle dynamic topography, then thinning factors calculated using subsidence analysis will be underestimated and less than those from gravity inversion. If present-day dynamic topography is known then a correction for it may be applied to the water-loaded subsidence from flexural backstripping, prior to conversion into lithosphere thinning factors. An example of this is shown in Fig. 5(c), where a correction for +500 m present-day dynamic uplift has been applied. A present-day dynamic uplift of +500 m is consistent with the difference between the distal oceanic sediment-corrected RDA and the crustal thickness component RDA shown in Fig. 4(b) (see Cowie *et al.* 2015 for further discussion on methodology).

3.4 Joint inversion of seismic and gravity data

Joint inversion of Moho depth using gravity and time domain seismic reflection data can be used to calculate the lateral variations in basement density and seismic velocity across the seismic profile. This joint inversion methodology described by Cowie *et al.* (2016) determines the combination of basement seismic velocities and densities needed to match the gravity inversion Moho with the interpreted seismic Moho in TWTT.

In the joint inversion process, first the Moho depth calculated from the gravity inversion (Fig. 6a) is converted into TWTT using a seismic velocity corresponding to the basement. Basement density and seismic velocity are linked by the empirical linear relationship defined by Birch (1964), $V_p = 2.27{*}\rho + 0.25$. The initial basement density of 2850 kg m^{-3} used in the gravity inversion corresponds to a seismic velocity of 6.72 km s^{-1}. The gravity Moho depth (in time) is then compared to a seismic interpretation of the Moho made in the time domain (Fig. 6b). Differences between the two Moho's in the time domain arise due to heterogeneities of the basement density and seismic velocity of the crustal basement. By laterally varying the basement density and seismic velocity, the gravity Moho (in time) is adjusted to fit the observed seismic Moho. The fit is achieved by iterative modifications of the basement density used in the gravity inversion to give Moho depth and the corresponding modifications to basement seismic velocity. The result of the joint inversion are the profiles of the lateral variation in basement density and seismic velocity. Figs 6(c) and (d) show profiles of laterally varying average basement density and seismic velocity predicted by the joint inversion of the gravity and seismic Moho data. Basement densities predicted for the distal section of the seismic profile reach values of 2900 kg m^{-3} consistent with densities for oceanic crust (Carlson and Herrick, 1990). In contrast, basement densities for the 9 km thick crust are noticeably less reaching a low of 2750 kg m^{-3}. In the region of exhumed mantle, it is not possible to determine basement density or seismic velocity from joint inversion because no seismic Moho is visible. The low basement densities in the proximal domain may indicate that significant thicknesses of sediment are present beneath the top basement seismic interpretation.

4 RESULTS

4.1 Testing top basement surface interpretations

Our seismic observations identified two possible candidates for top basement in the region interpreted as exhumed mantle. One interpretation is the deep top basement surface situated at the base of a faulted set of parallel reflectors at ~12 km depth (Fig. 7a), which we interpret as being sedimentary material. In contrast, the shallow top basement surface is interpreted to lie at the base of passive infill

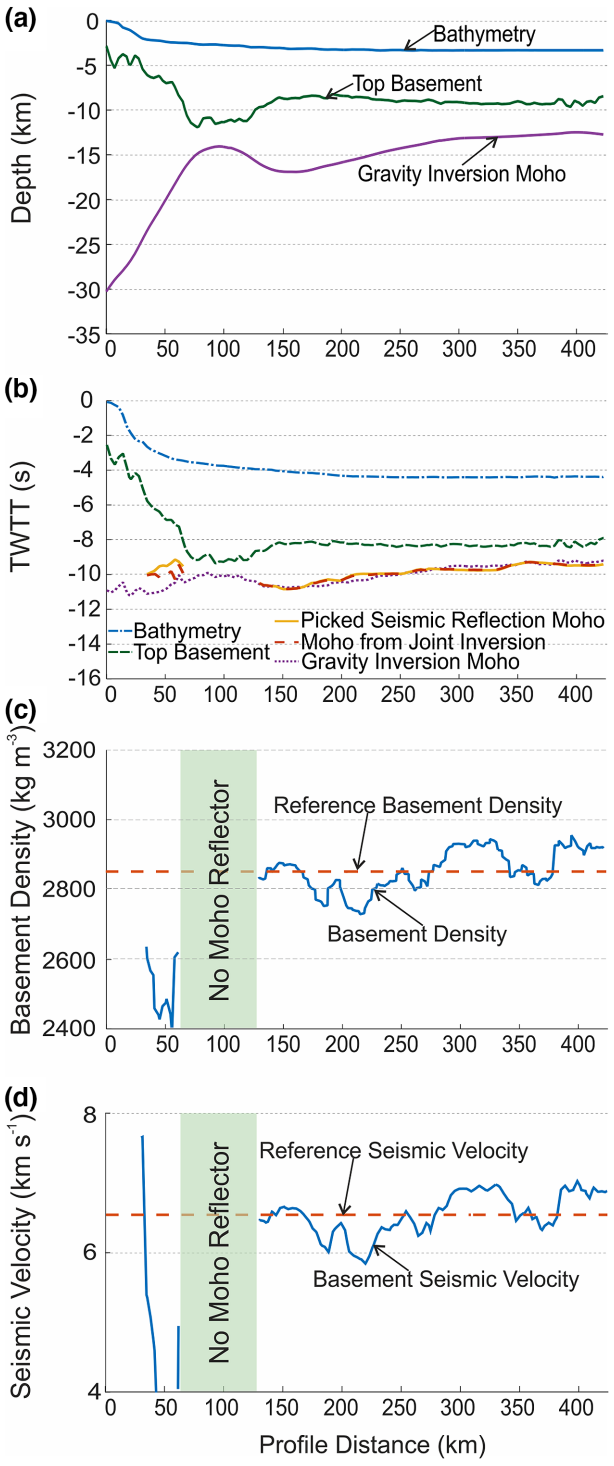

Figure 6. Joint gravity and seismic inversion results for the deep top basement surface: (a) Gravity inversion depth section using deep top basement surface. (b) Two-way traveltime (TWTT) cross-section showing the gravity inversion Moho, picked seismic reflection Moho and joint inversion Moho. (c) Average crustal basement density variation resulting from the joint inversion. (d) Average basement seismic velocity variation resulting from the joint inversion.

(Fig. 7b) at ∼9 km depth. We examine the differences and implications of using the two different top basement interpretations in our quantitative analysis.

Fig. 7 shows and compares results from gravity inversion and RDA analysis using the two different interpretations of top basement surface. The deeper top basement surface at the base of the parallel reflectors produces a gravity inversion Moho and crustal basement thickness shown in Fig. 7(a). Between 75 and 125 km the gravity Moho shallows to ∼14 km, which is ∼3 km below the picked top basement.

Placing top basement at the base of passive infill, ∼2 km shallower than the deep top basement interpretation, produces the gravity inversion Moho shown in Fig. 7(b). The gravity Moho shows a varying topography across the profile with a similar pattern to Fig. 7(a). They differ though between 75 and 125 km where the gravity Moho is deeper at 15–16 km giving a crustal thickness of ∼5 km.

The region between 75 and 125 km where the Moho depth and crustal thickness from gravity inversion differ corresponds to the region that has previously been interpreted as exhumed mantle (Nemčok *et al.* 2013; Sinha *et al.* 2015; Haupert *et al.* 2016). The difference in crustal thickness from gravity inversion using the two different top basement interpretations is ∼2 km. The deep top basement surface gives a crustal thickness of ∼3 km. This crustal thickness is equivalent to the mass deficiency of serpentinized mantle with respect to the mantle (Cowie *et al.* 2015). In contrast, the shallow top basement surface gives a crustal thickness of ∼5 km that is too deep for our solution to be interpreted as exhumed serpentinized mantle. This gravity inversion solution using the shallow top basement surface implies a thin layer of crustal basement in addition to serpentinized mantle, or alternatively, a 5 km thick layer of crustal basement with no serpentinized mantle. No exhumation of mantle rocks is predicted using the shallow top basement surface

The associated thinning factors from gravity inversion calculated for the deep top basement surface (Fig. 7c) reach a maximum crustal thinning between 75 and 125 km implying the complete removal of continental crust, consistent with the interpretation of exhumed mantle. Thinning factors for the shallow top basement surface (Fig. 7d) in a serpentinized mantle solution are less than 0.8, which is too low for complete continental crustal thinning to have occurred, implying the presence of some crustal material.

RDA results between 75 and 125 km for the deep top basement surface are negative (Fig. 7e), implying crust is thinner than 7 km or absent, consistent with the signal expected by exhumed mantle. RDA results for the shallow top basement surface (Fig. 7f) are positive (∼200 m) showing that the crust at this point is thicker than average 7 km thick oceanic crust, a signal that is not indicative of exhumed mantle but consistent with the presence of very thin continental crust.

4.2 Geological scenarios

Resolving the magmatic budget cannot be done unambiguously which leads to several potential interpretations and implications for the estimation of magmatic volume (Tugend *et al.* 2018). We present five geological scenarios (Fig. 8) that are consistent with the integrated quantitative analysis. The interpretations are deliberately kept simple and are presented as end-members. Each scenario contains at least one feature that corresponds to previous studies and/or seismic interpretations such as exhumed, serpentinized mantle (Nemčok *et al.* 2013; Haupert *et al.* 2016) or hyperextended

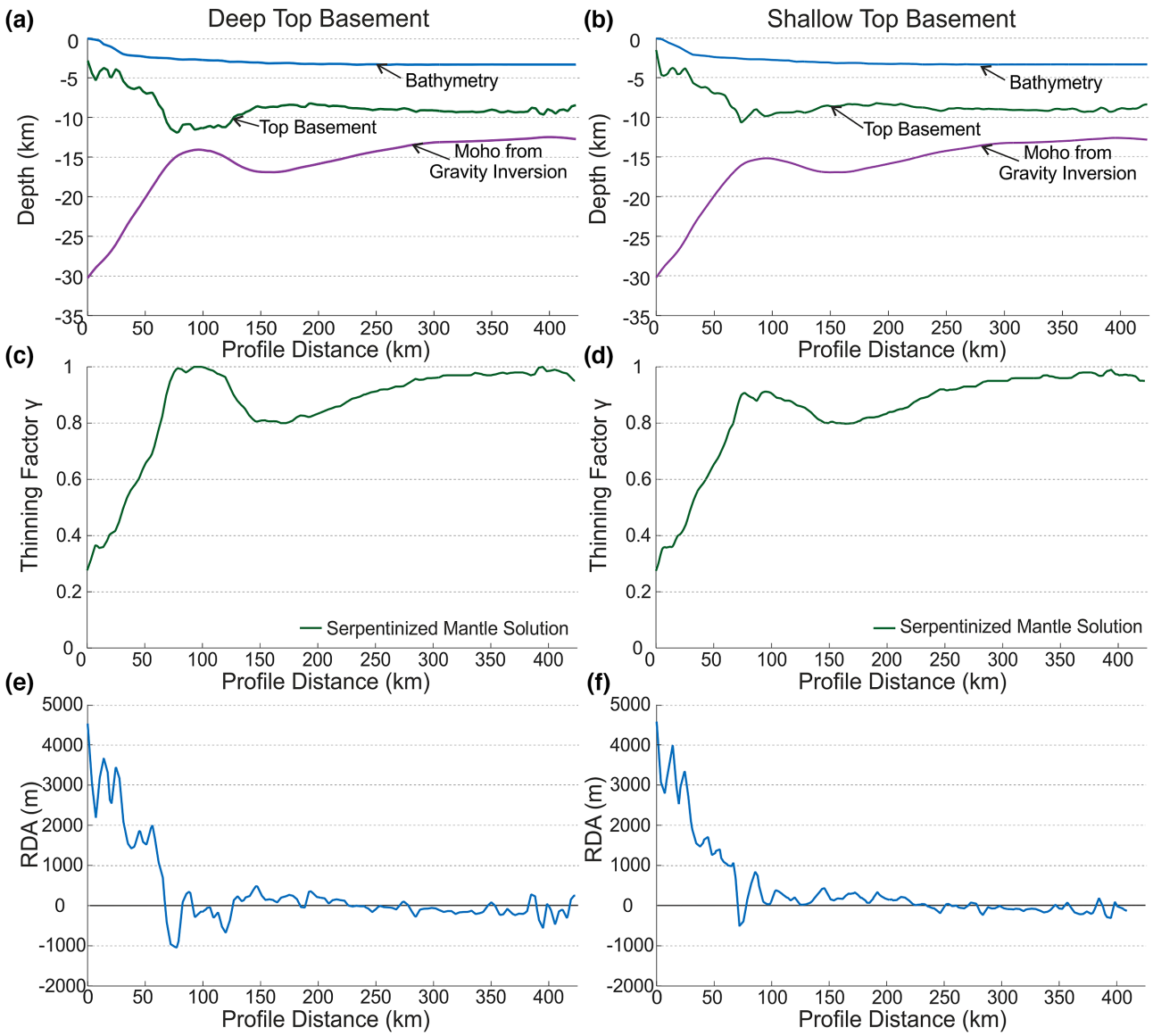

Figure 7. Testing top basement surfaces: (a) Gravity inversion cross-section showing depth to the Moho using the deeper top basement surface below the package of parallel faulted reflectors. (b) Gravity inversion cross-section showing depth to the Moho using the shallower top basement surface above the package of parallel faulted reflectors. (c) Lithosphere thinning factors associated with the gravity inversion shown in (a). (d) Lithosphere thinning factors associated with the gravity inversion in (b). (e) Residual depth anomaly analysis for deep top basement surface. (f) Residual depth anomaly analysis for shallow top basement surface.

continental crust (Pindell *et al.* 2014). We also include two of the scenarios previously presented in Tugend *et al.* (2018) to test the nature of the transitional crust: such as thick magmatic crust (Fig. 8a) or serpentinized mantle sandwiched between extrusive and intrusive additions (Fig. 8c).

Fig. 8(a) displays exhumed serpentinized mantle beneath extensionally faulted sediments that are covered by passive infill. The thick crust is composed entirely of magmatic material that transitions into normal oceanic crust with an average thickness of 5 km.

Fig. 8(b) also shows exhumed serpentinized mantle beneath extensionally faulted sediments that are covered by passive infill. However, the more distal thick crust is a fragment of continental crust formed during breakup. The transition from this continental crustal fragment to oceanic crust would likely be accompanied by extrusive and intrusive magmatic additions.

Another scenario is termed the 'sandwich' scenario (Fig. 8c; Gillard *et al.* 2017; Tugend *et al.* 2018) as it features serpentinized exhumed mantle and its associated sedimentary cover sandwiched between extrusive and intrusive magmatic additions. In this scenario, the exhumed mantle is progressively intruded oceanwards before transitioning into thin oceanic crust.

An alternative to exhumed serpentinized mantle is the presence of hyperextended continental crust sitting atop serpentinized mantle material that is not exhumed to the seafloor (Fig. 8d; see also Pindell *et al.* 2014). The outboard region of thick crust is represented as entirely magmatic in this scenario.

A final scenario (Fig. 8e) shows hyperextended continental crust atop serpentinized mantle material adjacent to a continental fragment.

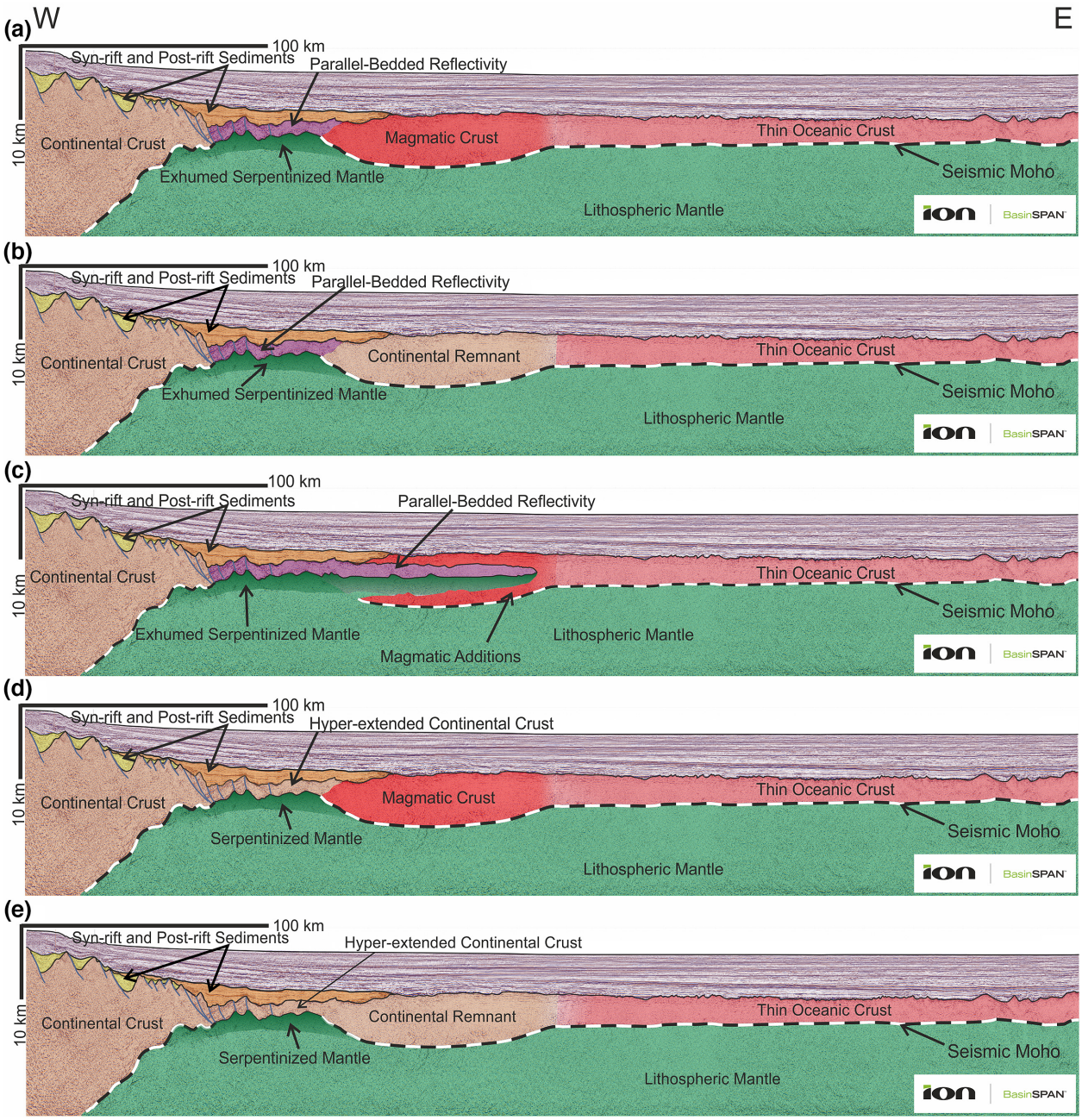

Figure 8. Geological interpretations of INE1-1000 based on initial seismic observations, previous interpretations from other studies (Nemčok *et al.* 2013; Sinha *et al.* 2015 and Haupert *et al.* 2016) and initial quantitative results. (a) Geological interpretation consisting of thinned continental crust transitioning into exhumed mantle, below parallel-bedded reflectivity, shifting to thick magmatic crust for ∼100 km followed by thin oceanic crust. (b) Geological interpretation consisting of thinned continental crust transitioning into exhumed mantle, below parallel-bedded reflectivity, transitioning into a continental remnant approximately 100 km wide before transitioning into thin oceanic crust. (c) 'Sandwich' scenario, similar to (a), but with the thick crust cored with exhumed serpentinized mantle (topped with sediments). (d) Geological interpretation consisting of thinned continental crust transitioning into hyperextended continental crust, transitioning into thick magmatic crust for ∼100 km followed by thin oceanic crust. (e) Geological interpretation consisting of thinned continental crust transitioning into hyperextended continental crust, shifting to a continental remnant approximately 100 km wide before transitioning into thin oceanic crust.

5 DISCUSSION

In this section we discuss the various geological interpretations, described above, in conjunction with the results of the quantitative analysis and the regional plate kinematic history. Our preferred final interpretation is that of Fig. 8(a) for which we give reasons below. In addition, we argue for the dismissal of the other five scenarios (Fig. 8b–e).

Both Figs 8(d) and (e) display hyperextended continental crust arising from the crustal thickness estimates in the gravity inversion using the shallow top basement surface and the interpretation of Pindell *et al.* (2014). Seismic observations (Fig. 2) show a reflective package below the shallow top basement surface that contains parallel-bedded reflectors, indicative of sedimentary material, not continental crust. It is for this reason that we dismiss the geological scenarios presented in Figs 8(d) and (e).

Figs 8(a)–(c) display exhumed, serpentinized mantle consistent with using the deep top basement surface in the gravity inversion to determine crustal basement thickness. These scenarios differ in their interpretation of the thick crust between exhumed mantle and oceanic crust, but all are consistent with results from the integrated quantitative analysis. We distinguish between them using seismic observations and the regional plate kinematic history.

Fig. 8(b) shows a continental crust fragment between exhumed mantle and oceanic crust. This implies a jump of rifting prior to breakup and seafloor spreading in order to isolate the continental fragment. As discussed in Section 1.1.1 there is evidence for an ocean ridge jump from between India/Elan Bank and Antarctica to the north between India and Elan Bank. If the interpretation shown in Fig. 8(b) was correct, then the conjugate margin on the north-west side of Elan Bank should also show a transition from thinned continental crust to oceanic crust. However, interpretation of seismic reflection data from north Elan Bank (Sinha *et al.* 2015) shows a transition from thin continental crust to exhumed mantle and then to oceanic crust (see fig. 5 in Sinha *et al.* 2015). This suggests that the interpretation shown in Fig. 8(b) is not consistent with observations.

The interpretation presented in Fig. 8(c) is similar to that proposed by Tugend *et al.* (2018). In this scenario the region of thicker crust between exhumed serpentinized mantle and oceanic crust consists of magmatic material that is extruded over and intruded within, exhumed, serpentinized mantle with a cover of sedimentary material. In this scenario the exhumation of serpentinized mantle is accompanied by a progressive increase in decompression melt production that produces a 'sandwich' of exhumed serpentinized mantle with extrusive volcanic material above and intrusive magmatic material below (Tugend *et al.* 2018). This scenario requires a single breakup event with a gradual increase in the volume of decompression melting. This complex basement transition to oceanic crust was initially suggested to occur at the conjugate Australia and Antarctica margins by Gillard *et al.* (2015). Our seismic observations (Fig. 2) do not show reflectivity suggestive of a 'sandwich' despite having good visibility down to the Moho. Seismic reflection data does not image these transitions well, one exceptional example from offshore West Africa (see Fig. 2 in Gillard *et al.* 2017) displays this reflectivity but their interpretation often relies on analogues preserved in onshore remnants. Although our quantitative analysis cannot exclude the presence of an exhumed mantle 'sandwich', it is not supported by our seismic observations suggesting that this model is not applicable to the East Indian rifted margin.

Our preferred scenario, shown in Fig. 8(a), interprets the composition of the 9 km thick crust between exhumed mantle and oceanic crust as thick magmatic crust. Fig. 9 shows the crustal cross-section from gravity inversion, the RDA analysis, thinning factor from gravity inversion and subsidence analysis and basement density from joint inversion of gravity and seismic reflection data that support this preferred interpretation. There is no single parametrization of decompression melting within the gravity inversion and subsidence analysis that fully explains the seismic observations or fits with the geological interpretations for INE1-1000. Therefore, the preferred solution is a composite interpretation of the different melt parametrizations as shown in Fig. 9(a). From continent to ocean the preferred composite of decompression melt parametrization is as follows: magma-poor (0–55 km), serpentinized mantle (55–105 km), magma-rich (105–285 km) and 'normal' magmatic (285–423 km). Our gravity inversion melting parametrization representing 'magma-rich' rifting over the thick, crustal area (Fig. 9a) is consistent with previous interpretations as well as seismic observations (Fig. 2d) that depict various intrusive magmatic features and extrusive features such as volcanoes and dipping reflector sequences. RDA analysis results over the thick crustal area are positive (Fig. 9b) indicating the crust is thicker than normal oceanic crust. Both gravity inversion and subsidence analysis lithosphere thinning factors reach 1.0 at the onset of the thick crust, implying the absence of continental material (Fig. 9c). Joint inversion of seismic and gravity data (Fig. 9d) show that the density of the 9 km thick crust between exhumed mantle and oceanic crust is less than that of the distal oceanic crust whose density is as expected for oceanic crustal basement (Carlson & Herrick 1990). This lower density for the 9 km thick crust suggests the presence of lighter material possibly sedimentary material or volcaniclastics. This is supported by seismic observations (Fig. 2) that indicate the presence of volcanoes at the top of the thick crust as well as dipping reflector sequences, which could be sources for volcaniclastic material.

The juxtaposition of exhumed mantle and thick magmatic crust, as shown in Figs 8(a) and 9, can be explained by the known reorganization of seafloor spreading, via an ocean ridge jump, from the Enderby Basin, between Elan Bank and Antarctica northwards, to between India and Elan Bank (Gaina *et al.* 2003, 2007). A reorganization of seafloor spreading into pre-existing exhumed mantle would place newly formed magmatic crust next to the exhumed mantle. The development of proto-Kerguelen mantle plume magmatism at the time of India–Antarctica lithospheric breakup (Olierook *et al.* 2016) could explain decompression melting exceeding that of normal seafloor spreading (7 km; White *et al.* 1992) leading to thicker magmatic crust. This same development of the proto-Kerguelen mantle plume may also be a contributing factor to the ocean ridge jump.

In our interpretation, the scenario shown in Figs 8(a) and 9, containing thick magmatic crust outboard of exhumed mantle is not due to the inherent evolution of exhumed, serpentinized mantle into magmatic crust caused by the escape of retained melt (Lizarralde *et al.* 2004). Instead, the juxtaposition of exhumed mantle and thick magmatic crust is a result of a seafloor spreading reorganization into exhumed mantle coinciding with an asthenosphere temperature anomaly.

By combining seismic observations, quantitative analysis and regional plate kinematic history we are able to dismiss alternative scenarios, arriving at a single favoured interpretation where the East Indian rifted margin preserves exhumed mantle juxtaposed to thick, magmatic crust. Classifying the East Indian rifted margin, in particular the Krishna–Godavari Basin, as magma-poor suggests little magmatism during rifting and breakup. However, the results presented within this study suggest that it is not a simple end-member rifted margin, instead displaying both magma-poor and magma-rich characteristics.

6 SUMMARY

Establishing the volume of magmatic crust on a margin using quantitative methods is important in distinguishing margin type. Yet, the classification of end-member magmatic rifted margin types is often assumed based on a morphological features interpreted from seismic data without the use of quantitative validation. ION line INE1-1000 is often described as a 'classic' magma-poor margin based on seismic interpretation alone. However, we have demonstrated that, by using an integrated set of geophysical techniques, thick magmatic crust may separate exhumed serpentinized mantle

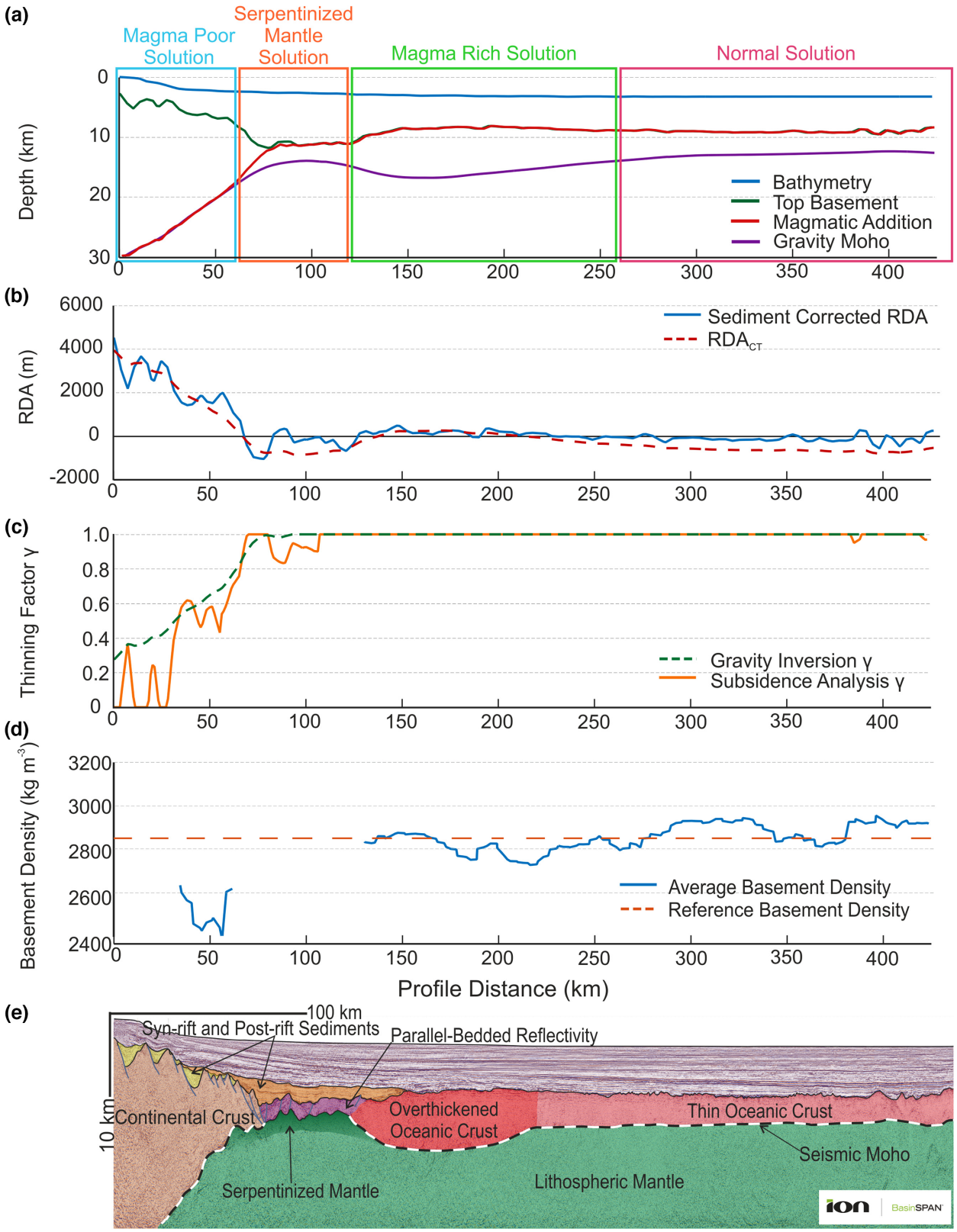

Figure 9. Integrated quantitative analysis (IQA) results for seismic line INE1-1000, combining gravity inversion, RDA analysis, subsidence analysis and joint inversion results. (a) Composite cross-section from gravity inversion decompression melting parametrizations using the deep top basement surface. (b) RDA result for the sediment-corrected bathymetry using depp top basement surface and RDA component from crustal thickness variations. (c) Thinning factor results from subsidence analysis and from the composite gravity inversion. (d) Joint inversion of gravity and seismic Moho data showing lateral basement density variations across the profile. (e) Preferred geological interpretation based on quantitative results and seismic observations showing exhumed mantle below parallel-bedded reflectivity and thick magmatic crust transitioning into thin oceanic crust.

and oceanic crust. Our quantitative analysis consists of gravity inversion, residual depth anomaly analysis, subsidence analysis and joint inversion of gravity and seismic reflection data alongside seismic observations. This analysis together with the plate kinematic history of the region, indicates that the thick crust separating exhumed mantle and oceanic crust on the East Indian rifted margin is a result of polyphase rifting that is not genetically related to magma-poor continental breakup and seafloor spreading initiation. The first rift phase consisted of magma-poor rifting forming exhumed mantle, while the second phase of rifting resulted from a northwards reorganization of seafloor spreading, forming a 9 km thick magmatic crust. We find no evidence to suggest that the thick crust formed via the release of retained melt within the mantle and is therefore not related to magma-poor continental breakup and the transition to magmatic seafloor spreading. Our interpretation suggests that the East Indian rifted margin is not a simple end-member magma-poor margin, and instead has characteristics of both magma-poor and magma-rich rifted margins because of the ocean ridge jump. As both rift phases contributed towards the final rifted margin structure, using end-member terminology of magma-poor or magma-rich to classify the rifted margin is misleading.

ACKNOWLEDGEMENTS

We would like to thank the MM4 Industry Consortium who funded this work. We also thank the reviewers for their comments and recommendations, in particular Garry Karner.

REFERENCES

Alvey, A., Gaina, C., Kusznir, N.J. & Torsvik, T.H., 2008. Integrated crustal thickness mapping and plate reconstructions for the high Arctic, *Earth planet. Sci. Lett.,* **274,** 310–321.

Birch, F., 1964. Density and composition of mantle and core, *J. geophys. Res.,* **69,** 4377–4388.

Boillot, G., Feraud, G., Recq, M. & Giradeau, J., 1989. Undercrusting by serpentinite beneath rifted margins, *Nature,* **342,** 189–192.

Borissova, I., Coffin, M.F., Charvis, P. & Operto, S., 2003. Structure and development of a microcontinent: Elan Bank in the southern Indian Ocean, *Geochem. Geophys. Geosyst.,* **4,** 1–16.

Carlson, R.L. & Herrick, C.N., 1990. Densities and porosities in the oceanic crust and their variations with depth and age, *J. geophys. Res.,* **95,** 9153–9170.

Chand, S., Radhakrishna, M. & Subrahmanyam, C., 2001. India-East Antarctica conjugate margins: Rift-shear tectonic setting inferred from gravity and bathymetry data, *Earth planet. Sci. Lett.,* **185,** 225–236.

Chappell, A.R. & Kusznir, N.J., 2008. Three-dimensional gravity inversion for Moho depth at rifted continental margins incorporating a lithosphere thermal gravity anomaly correction, *Geophys. J. Int.,* **174,** 1–13.

Charvis, P. & Operto, S., 1999. Structure of the Cretaceous Kerguelen Volcanic Province (southern Indian Ocean) from wide-angle seismic data, *J. Geodyn.,* **28,** 51–71.

Charvis, P., Recq, M., Operto, S. & Brefort, D., 1995. Deep structure of the northern Kerguelen Plateau and hotspot-related activity, *Geophys. J. Int.,* **122,** 899–924.

Christensen, M.I. & Mooney, W.D., 1995. Seismic velocity structure and composition of the continental crust - a global view, *J. geophys. Res. Earth,* **100,** 9761–9788.

Coffin, M.F., Storey, M., Müller, R.D., Gahagan, L.A., Pringle, M.S., Duncan, R.A. & Gladczenko, T.P., 2002. Kerguelen hotspot magma output since 130 Ma., *J. Petrol.,* **43,** 1121–1139.

Cooper, C., 2010. Anomalous bathymetry and mass heterogeneity at the conjugate Iberia and Newfoundland rifted margins, *PhD thesis*, University of Liverpool, Liverpool, 260 pp.

Cowie, L., Angelo, R.M., Kusznir, N.J., Manatschal, G. & Horn, B., 2016. Structure of the ocean–continent transition, location of the continent-ocean boundary and magmatic type of the northern Angolan margin from integrated quantitative analysis of deep seismic reflection and gravity anomaly data, *Geol. Soc. London Spec. Publ.,* **438,** 159–176.

Cowie, L., Kusznir, N.J. & Manatschal, G., 2015. Determining the COB location along the Iberian margin and Galicia Bank from gravity anomaly inversion, residual depth anomaly and subsidence analysis, *Geophys. J. Int.,* **203,** 1355–1372.

Crosby, A.G. & McKenzie, D., 2009. An analysis of young ocean depth, gravity and global residual topography, *Geophys. J. Int.,* **178,** 1198–1219.

Doré, T. & Lundin, E., 2015. Hyperextended continental margins — Knowns and unknowns, *Geology,* **43,** 95–96.

Fletcher, R., Kusznir, N.J. & Cheadle, M., 2009. Melt initiation and mantle exhumation at the Iberian rifted margin: comparison of pure-shear and upwelling-divergent flow models of continental breakup, *C. R. Geosci.,* **341,** 394–405.

Franke, D., 2013. Rifting, lithosphere breakup and volcanism: comparison of magma-poor and volcanic rifted margins, *Mar. Pet. Geol.,* **43,** 63–87.

Frey, F.A. *et al.* 2000. Origin and evolution of a submarine large igneous province: the Kerguelen Plateau and Broken Ridge, southern Indian Ocean, *Earth planet. Sci. Lett.,* **176,** 73–89.

Gaina, C., Müller, R.D., Brown, B. & Ishihara, T., 2003. Microcontinent formation around Australia, *Geol. Soc. Am. Spec. Pap.,* **372** 405–416.

Gaina, C., Müller, R.D., Brown, B., Ishihara, T. & Ivanov, S., 2007. Breakup and early seafloor spreading between India and Antarctica, *Geophys. J. Int.,* **170,** 151–169.

Geoffroy, L., 2005. Volcanic passive margins, *C. R. Geosci.,* **337,** 1395–1408.

Gibbons, A.D., Whittaker, J.M. & Müller, R.D., 2013. The breakup of East Gondwana: assimilating constraints from Cretaceous ocean basins around India into a best-fit tectonic model, *J. geophys. Res.,* **118,** 808–822.

Gillard, M., Autin, J. & Manatschal, G., 2016. Fault systems at hyper-extended rifted margins and embryonic oceanic crust: structural style, evolution and relation to magma, *Mar. Pet. Geol.,* **76,** 51–67.

Gillard, M., Autin, J., Manatschal, G., Sauter, D., Munschy, M. & Schaming, M., 2015. Tectonomagmatic evolution of the final stages of rifting along the deep conjugate Australian–Antarctic magma-poor rifted margins: constraints from seismic observations, *Tectonics,* **34,** 753–783.

Gillard, M., Sauter, D., Tugend, J., Tomasi, S., Epin, M.E. & Manatschal, G., 2017. Birth of an oceanic spreading center at a magma-poor rift system, *Sci. Rep.,* **7,** doi:10.1038/s41598-017-15522-2.

Greenhalgh, E.E. & Kusznir, N.J., 2007. Evidence for thin oceanic crust on the extinct Aegir Ridge, Norwegian Basin, NE Atlantic derived from satellite gravity inversion, *Geophys. Res. Lett.,* **34,** 1–5.

Haupert, I., Manatschal, G., Decarlis, A. & Unternehr, P., 2016. Upper-plate magma-poor rifted margins: stratigraphic architecture and structural evolution, *Mar. Pet. Geol.,* **69,** 241–261.

Ingle, S., Weis, D. & Frey, F.A., 2002a. Indian continental crust recovered from Elan bank, Kerguelen plateau (ODP Leg 183, Site 1137), *J. Petrol.,* **43,** 1241–1257.

Ingle, S., Weis, D., Scoates, J.S. & Frey, F.A., 2002b. Relationship between the early Kerguelen plume and continental flood basalts of the paleo-Eastern Gondwanan margins, *Earth planet. Sci. Lett.,* **197,** 35–50.

Kusznir, N. & Karner, G., 1985. Dependence of the flexural rigidity of the continental lithosphere on rheology and temperature, *Nature,* **316,** 138–142.

Kusznir, N.J., Roberts, A.M. & Alvey, A.D., 2018. Crustal structure of the conjugate Equatorial Atlantic Margins, derived by gravity anomaly inversion, *Geol. Soc. London Spec. Publ.,* **476,** doi:10.1144/SP476.5.

Kusznir, N.J., Roberts, A.M. & Morley, C.K., 1995. Forward and reverse modelling of rift basin formation, *Geol. Soc. London Spec. Publ.,* **80,** 33–56.

Lal, N.K., Siawal, A. & Kaul, A.K., 2009. Evolution of east coast of India – a plate tectonic reconstruction, *J. Geol. Soc. India,* **73,** 249–260.

Lizarralde, D., Gaherty, J.B., Collins, J.A., Hirth, G. & Kim, S.D., 2004. Spreading-rate dependence of melt extraction at mid-ocean ridges from mantle seismic refraction data, *Nature,* **432,** 744–747.

Lundin, E.R. & Doré, A.G., 2011. Hyperextension, serpentinization, and weakening: a new paradigm for rifted margin compressional deformation, *Geology,* **39,** 347–350.

Magee, C., Maharaj, S.M., Wrona, T. & Jackson, C.A.L., 2015. Controls on the expression of igneous intrusions in seismic reflection data, *Geosphere,* **11,** 1024–1041.

Magee, C. *et al.* 2018. Magma plumbing systems: a geophysical perspective, *J. Petrol.,* **59,** 1217–1251.

McKenzie, D., 1978. Some remarks on the development of sedimentary basins, *Earth planet. Sci. Lett.,* **40,** 25–32.

Mckenzie, D. & Bickle, M.J., 1988. The volume and composition of melt generated by extension of the lithosphere, *J. Petrol.,* **29,** 625–689.

Müller, R.D., Gaina, C., Roest, W.R. & Hansen, D.L., 2001. A recipe for microcontinent formation, *Geology,* **29,** 203–206.

Müller, R.D., Gaina, C., Tikku, A., Mihut, D., Cande, S.C. & Stock, J.M., 2000. Mesozoic/Cenozoic tectonic events around Australia, *Hist. Dyn. Glob. Plate Motions,* **121,** 161–188.

Müller, R.D., Roest, W.R., Royer, J.Y., Gahagan, L.M. & Sclater, J.G., 1997. Digital isochrons of the world's ocean floor, *J. geophys. Res.,* **102,** 3211–3214.

Müller, R.D., Sdrolias, M., Gaina, C. & Roest, W.R., 2008. Age, spreading rates, and spreading asymmetry of the world's ocean crust, *Geochem. Geophys. Geosyst.,* **9,** 1–19.

Nemčok, M. *et al.* 2013. East Indian margin evolution and crustal architecture: integration of deep reflection seismic interpretation and gravity modelling, *Geol. Soc. London Spec. Publ.,* **369,** 477–496.

Nicolaysen, K.E., Bowring, S., Frey, F.A., Weis, D., Ingle, S., Pringle, M.S. & Coffin, M.F., 2001. Provenance of proterozoic garnet-biotite gneiss recovered from Elan Bank, Kerguelen Plateau, southern Indian Ocean, *Geology,* **29,** 235–238.

Olierook, H.K.H., Jourdan, F., Merle, R.E., Timms, N.E., Kusznir, N.J. & Muhling, J.R., 2016. Bunbury Basalt: Gondwana breakup products or earliest vestiges of the Kerguelen mantle plume? *Earth planet. Sci. Lett.,* **440,** 20–32.

Parker, R.L., 1972. The rapid calculation of potential anomalies, *Geophys. J. R. Astron. Soc.,* **31,** 447–455.

Pickup, S.L.B., Whitmarsh, R.B., Fowler, C.M.R. & Reston, T.J., 1996. Insight into the nature of the ocean-continent transition off West-Iberia from a deep-multichannel seismic reflection profile, *Geology,* **24,** 1079–1082.

Pindell, J., Graham, R. & Horn, B., 2014. Rapid outer marginal collapse at the rift to drift transition of passive margin evolution, with a Gulf of Mexico case study, *Basin Res.,* **26,** 701–725.

Planke, S., Rasmussen, T., Rey, S.S. & Myklebust, R., 2005. Seismic characteristics and distribution of volcanic intrusions and hydrothermal vent complexes in the Vøring and Møre basins, *Geol. Soc. London Spec. Publ.,* **6,** 833–844.

Pérez-Gussinyé, M., 2013. A tectonic model for hyperextension at magma-poor rifted margins: an example from the West Iberia – Newfoundland conjugate margins, *Geol. Soc. London Spec. Publ.,* **369,** 403–427.

Pérez-Gussinyé, M., Morgan, J.P., Reston, T.J. & Ranero, C.R., 2006. The rift to drift transition at non-volcanic margins: insights from numerical modelling, *Earth planet. Sci. Lett.,* **244,** 458–473.

Radhakrishna, M., Twinkle, D., Nayak, S., Bastia, R. & Rao, G.S., 2012. Crustal structure and rift architecture across the Krishna–Godavari basin in the central Eastern Continental Margin of India based on analysis of gravity and seismic data, *Mar. Pet. Geol.,* **37,** 129–146.

Ramana, M. V., Ramprasad, T. & Desa, M., 2001. Sea floor spreading magnetic anomalies in the Enderby Basin, East Antarctica, *Earth planet. Sci. Lett.,* **191,** 241–255.

Ramana, M.V. *et al.* 1994. Mesozoic anomalies in the Bay of Bengal, *Earth planet. Sci. Lett.,* **121,** 469–475.

Reston, T.J., 2009. The structure, evolution and symmetry of the magma-poor rifted margins of the North and Central Atlantic: a synthesis, *Tectonophysics,* **468,** 6–27.

Reston, T.J. & Manatschal, G., 2011. Chapter 1, Rifted margins: building blocks of later collision, in: *Arc-Continent Collions,* pp. 3–21, eds, Brown, D. &, Ryan P. D., Springer, Switzerland, doi:10.1007/978-3-540-88558-0.

Roberts, A.M., Kusznir, N.J., Corfield, R.I., Thompson, M. & Woodfine, R., 2013. Integrated tectonic basin modelling as an aid to understanding deep-water rifted continental margin structure and location, *Geol. Soc. London Spec. Publ.,* **19,** 65–88.

Roberts, A.M., Kusznir, N.J., Yielding, G. & Styles, P., 1998. 2D flexural backstripping of extensional basins: the need for a sideways glance, *Petroleum Geoscience,* **4,** 327–338.

Royer, J.Y. & Coffin, M.F., 1988. Jurassic to eocene plate tectonic reconstructions in the Kerguelen plateau Region, *Proc. Ocean Drill. Progr. Sci. Results,* Vol. 120, doi: 10.2973/odp.proc.sr.120.200.1992.

Sandwell, D. & Smith, W.H., 2009. Global marine gravity from retracked Geosat and ERS-1 altimetry: ridge segmentation versus spreading rate, *J. geophys. Res.,* **114,** 1–18.

Sawyer, D.S., Coffin, M.F., Reston, T.J., Stock, J.M. & Hopper, J.R., 2007. COBBOOM: the Continental Breakup and Birth of Oceans Mission, *Sci. Drill.,* **5,** 13–25.

Schofield, N., Heaton, L., Holford, S.P., Archer, S.G., Jackson, C.A.-L. & Jolley, D.W., 2012. Seismic imaging of "broken bridges": linking seismic to outcrop-scale investigations of intrusive magma lobes, *J. Geol. Soc. London,* **169,** 421–426.

Sclater, J.G. & Christie, P.A.F., 1980. Continental stretching: An explanation of the Post-Mid-Cretaceous subsidence of the central North Sea Basin, *J. geophys. Res.,* **85,** 3711–3739.

Sinha, S.T., Nemčok, M., Choudhuri, M., Sinha, N. & Rao Pundarika, D., 2015. The role of break-up localization in microcontinent separation along a strike-slip margin: the East India – Elan Bank case study, *Geol. Soc. London Spec. Publ.,* **431,** doi: 10.1144/SP431.5.

Smith, R.A., 1961. A uniqueness theorem concerning gravity fields, *Math. Proc. Cambridge Philos. Soc.,* **57,** 865–870.

Smith, W.H. & Sandwell, D., 1997. Global sea floor topography from satellite altimetry and ship depth soundings, *Science,* **277,** 1956–1962.

Soares, D.M., Alves, T.M. & Terrinha, P., 2012. The breakup sequence and associated lithospheric breakup surface: their significance in the context of rifted continental margins (West Iberia and Newfoundland margins, North Atlantic), *Earth planet. Sci. Lett.,* **355–356,** 311–326.

Sutra, E., Manatschal, G., Mohn, G. & Unternehr, P., 2013. Quantification and restoration of extensional deformation along the Western Iberia and Newfoundland rifted margins, *Geochem. Geophys. Geosyst.,* **14,** 2575–2597.

Tucholke, B.E., Behn, M.D., Buck, W.R. & Lin, J., 2008. Role of melt supply in oceanic detachment faulting and formation of megamullions, *Geology,* **36,** 455–458.

Tucholke, B.E., Sawyer, D.S. & Sibuet, J.C., 2007. Breakup of the Newfoundland Iberia rift, *Geol. Soc. London Spec. Publ.,* **282,** 9–46.

Tugend, J., Manatschal, G. & Kusznir, N.J., 2015. Spatial and temporal evolution of hyperextended rift systems: implication for the nature, kinematics, and timing of the Iberian-European plate boundary, *Geology,* **43,** 15–18.

Tugend, J. *et al.* 2018. Reappraisal of the magma-rich versus magma-poor rifted margin archetypes, *Geol. Soc. London Spec. Publ.,* **476,** doi.org/10.1144/SP476.9.

Warner, M.R., 1987. Seismic reflections from the Moho – the effect of isostasy, *Geophys. J. R. Astron. Soc.,* **88,** 425–435.

White, R.S. & McKenzie, D., 1989. Magmatism at rift zones: the generation of volcanic continental margins and flood basalts, *J. geophys. Res.,* **94,** 7685.

White, R.S., McKenzie, D. & O'Nions, R.K., 1992. Oceanic crustal thickness from seismic measurements and rare earth element inversions, *J. geophys. Res.,* **97,** 19683.

SUPPORTING INFORMATION

Supplementary data are available at *GJI* online.

Figure S1. Gravity inversion parametrization of decompression melting results for the shallow top basement surface: (a) 'Normal' magmatic solution, (b) Magma-poor solution, (c) Magma-rich solution, (d) Serpentinized mantle solution.
Please note: Oxford University Press is not responsible for the content or functionality of any supporting materials supplied by the authors. Any queries (other than missing material) should be directed to the corresponding author for the article.